Title

Optimal mechanical interactions direct multicellular network formation on elastic substrates

Journal

Proceedings of the National Academy of Sciences of the United States of America, 120(45)

ISSN

0027-8424

Authors

Noerr, Patrick S

Alvarado, Jose E Zamora

Golnaraghi, Farnaz

et al.

Publication Date

2023-11-07

DOI

10.1073/pnas.2301555120

PNAS RESEARCH ARTICLE | APPLIED PHYSICAL SCIENCES OPEN ACCESS

Optimal mechanical interactions direct multicellular network formation on elastic substrates

Patrick S. Noerr[a], Jose E. Zamora Alvarado[b], Farnaz Golnaraghi[a], Kara E. McCloskey[b], Ajay Gopinathan[a,1], and Kinjal Dasbiswas[a,1]

Edited by Ming Guo, Massachusetts Institute of Technology, Cambridge, MA; received February 6, 2023; accepted September 9, 2023 by Editorial Board Member Mehran Kardar

Cells self-organize into functional, ordered structures during tissue morphogenesis, a process that is evocative of colloidal self-assembly into engineered soft materials. Understanding how intercellular mechanical interactions may drive the formation of ordered and functional multicellular structures is important in developmental biology and tissue engineering. Here, by combining an agent-based model for contractile cells on elastic substrates with endothelial cell culture experiments, we show that substrate deformation–mediated mechanical interactions between cells can cluster and align them into branched networks. Motivated by the structure and function of vasculogenic networks, we predict how measures of network connectivity like percolation probability and fractal dimension as well as local morphological features including junctions, branches, and rings depend on cell contractility and density and on substrate elastic properties including stiffness and compressibility. We predict and confirm with experiments that cell network formation is substrate stiffness dependent, being optimal at intermediate stiffness. We also show the agreement between experimental data and predicted cell cluster types by mapping a combined phase diagram in cell density substrate stiffness. Overall, we show that long-range, mechanical interactions provide an optimal and general strategy for multicellular self-organization, leading to more robust and efficient realizations of space-spanning networks than through just local intercellular interactions.

mechanobiology | computational physics | soft matter | biomaterials | cell networks

Significance

Many animal cells actively generate mechanical forces while also sensing and responding to changes in their mechanical environment. This may drive cell–cell interactions through their mutual deformations of the surrounding elastic medium, which lead to self-organized multicellular structures. We show with modeling and experiments on endothelial cells cultured on soft substrates that cells may find and align with each other through such substrate stiffness–dependent mechanical interactions. We predict how network structural features relate to the transport functions of vascular networks and how these may be tuned by manipulating substrate mechanical properties. This understanding of multicellular network formation can guide tissue engineering applications, that require in vitro vascular network formation in order to be viable.

The morphogenesis of biological tissue involves the organization of cells into functional, self-assembled structures (1). The aggregation of cells into ordered structures requires effectively attractive cell–cell interactions (2). An example of such a process that is relevant to biological development, disease and tissue engineering, is the morphogenesis of blood vessels. This is initiated by patterned structures of endothelial cells (ECs), which align end to end to form elongated chains that intersect to give a branched morphology. Although the conditions required for vascular-like development in engineered in vitro systems are well established and EC vascular networks have been mathematically modeled using various approaches (3–9), the nature of the cell–cell interactions that drive the ECs to find each other to form networks and the dependence of these interactions on matrix stiffness have not been definitively identified.

The emergence of complex structures from the interactions of individual agents bears resemblance to colloidal self-assembly. For example, dipolar particles, such as ferromagnetic colloids, will align end-to-end into equilibrium, linear structures such as chains or rings (10). At higher densities, the chains intersect to form gel-like network structures (11). Such structures have been studied in simulation in the context of active dipoles representing synthetic active colloids endowed with a permanent or induced dipole moment (12–14) and swimming microorganisms (15) such as magnetotactic bacteria (16). Animal cells that adhere to and crawl on elastic substrates and interact through mechanical deformations of the substrate (17) are also expected to attract and align to form multicellular structures (18). Such mechanically directed self-organization of cells into functional structures, such as vascular networks, implies that network morphology depends on substrate stiffness.

While cells routinely communicate using chemical signals, they also sense each other through mechanical forces that they exert on each other, either through direct cell–cell contacts or indirectly, through mutual deformations of a compliant, extracellular substrate (19, 20). Large and measurable substrate deformations (21) are produced by many types of adherent cells. These use mechanical forces actively generated by myosin motors in their actin cytoskeleton to change shape, move, and sense their surroundings (22). Adherent cells ubiquitously induce contractile mechanical deformations in elastic media.

Author contributions: P.S.N., J.E.Z.A., K.E.M., A.G., and K.D. designed research; P.S.N., J.E.Z.A., F.G., A.G., and K.D. performed research; J.E.Z.A., F.G., and K.E.M. contributed new reagents/analytic tools; P.S.N. and J.E.Z.A. analyzed data; and P.S.N., K.E.M., A.G., and K.D. wrote the paper.

The authors declare no competing interest.

This article is a PNAS Direct Submission. M.G. is a guest editor invited by the Editorial Board.

[1]To whom correspondence may be addressed. Email: agopinathan@ucmerced.edu or kdasbiswas@ucmerced.edu.

This article contains supporting information online at https://www.pnas.org/lookup/suppl/doi:10.1073/pnas.2301555120/-/DCSupplemental.

Published November 1, 2023.

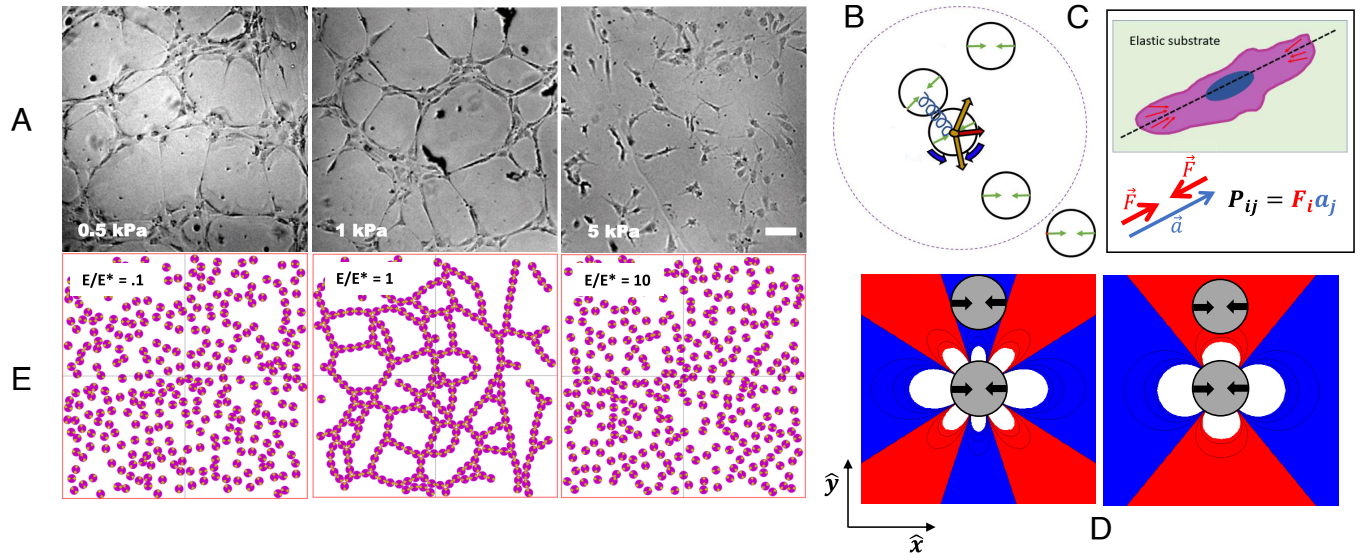

Fig. 1. Cell network formation is optimized by substrate stiffness. (*A*) Human umbilical vascular endothelial cells (HUVECs) cultured on polyacrylamide hydrogel substrates of varying stiffness that were coated with Matrigel. At high stiffness (5 kPa and glass), the cells did not form networks but did so on softer substrates (0.5 and 1 kPa) (Scale bar, 100 μm). Images reprinted with permission from ref. 43. (*B*) Cartoon of a simulation snapshot where green arrows indicate the cell's force dipole, the large purple dashed ring denotes the elastic interaction range, the blue squiggle indicates a repulsive spring to prevent overlap, bold gold arrows represent force vectors due to elastic interactions, the bold red arrows represent the net force vector on the central cell, the bold blue arrow represents torque on central cell due to elastic interaction with neighbors. (*C*) Cartoon cell deforming the surrounding elastic substrate by applying forces along a main axis. (*D*) u_{xx} component of the strain field caused by a contractile force dipole centered at the origin pinching along the x-axis for $\nu = 0.5$(*Left*) and $\nu = 0.1$(*Right*) with coordinate axes labeled. (*E*) Simulation snapshots of 300 cells modeled as contractile force dipoles that move and reorient according to substrate-mediated cell–cell elastic interaction forces. Cells form percolating networks only for a range of substrate stiffness values centered around an optimal stiffness, E^*, above which cells exert maximal traction force. For substrates around optimal stiffness ($E/E^* \sim 1$), the substrate-mediated cell–cell elastic interactions are maximal and can be much larger than the noise in cell movements, whereas for very soft ($E/E^* \ll 1$) or very stiff ($E/E^* \gg 1$) substrates, the elastic interactions are likely to be overwhelmed by noise, resulting in a lack of ordered structures.

The resulting intercellular communication is longer ranged, faster, and more general than chemical signaling which typically requires diffusive transport and specific chemical interactions. Elastic substrate–mediated intercellular mechanical communication has been demonstrated for several contractile cell types. For example, endothelial cells modulate their intercellular contact frequency according to substrate stiffness (23), cardiomyocytes synchronize their beating with substrate mechanical oscillations induced by a distant probe (24, 25), and fibroblasts interact at long range through their structural remodeling of fibrous extracellular media (26, 27).

Cells sense substrate mechanical deformations through mechanotransduction occurring at the biomolecular scale (28). Such cellular signaling is carried out by proteins associated with the cell–substrate adhesions, that are in turn connected to the cell's cytoskeletal force-generating machinery (21). At a coarse-grained level, the contractile apparatus of cells adhered to an extracellular substrate can be modeled as active elastic inclusions (29), which adapts the theory of material inclusions developed by Eshelby (30), to describe cellular contractility as force dipoles embedded in an elastic medium. This general theoretical approach predicts how multicellular and subcellular cytoskeletal organization depends on substrate stiffness (18, 31). It has been applied successfully to explain experimental observations of substrate stiffness–dependent structural order in a variety of cell types in a unified manner (32–36). While these previous works focused on the stationary configurations of elastic dipoles in the context of adherent cells (37, 38), we now consider cell self-assembly when the cellular dipoles are free to translate and rotate in response to mechanical forces, thereby serving as minimal models for contractile cells that adhere to, spread, and crawl on soft media. We show that cell–cell mechanical interactions mediated by a compliant elastic substrate can drive network formation and that the resulting network morphology is inherently sensitive to substrate stiffness.

Coarse-grained material properties of the cellular microenvironment, such as its stiffness and viscosity, are known to play crucial roles in determining cell structure and function (39–41), including for bacterial colonies (42). Recently, it was shown that human umbilical vascular endothelial cells (HUVECs) assemble into networks on softer substrates ($E \sim 1$ kPa) but fail to do so on stiffer substrates (Fig. 1*A*), independently of the type of hydrogel used (43). In contrast, it was shown in ref. 44 that, under certain conditions, bovine endothelial cells formed networks preferentially on stiffer substrates ($E \sim 10$ kPa). Both these experiments show that EC network formation is sensitive to substrate stiffness and therefore suggest that cell mechanical interactions mediated by the substrate are involved.

Model and Results

Substrate Stiffness–Dependent Endothelial Cell Network Organization Motivates Model for Cell Mechanical Interactions. To model cell network formation, we incorporate substrate-mediated cell mechanical interactions into an agent-based model for cell motility (45). This captures the dynamic rearrangements of cells into favorable configurations. In our agent-based approach (46, 47), summarized in Fig. 1*B*, we consider a system of N particles, each a disk of diameter d. Depending on the context, each disk could model a cell or its constituent parts, and their motion represents both cell migration as well as cell spreading or shape change dynamics. Details of the cell shape are not included in this minimal model. These model cells self-organize according to substrate friction–dominated

overdamped dynamics that depend on intercell interactions as well as individual cell stochastic movements described by an effective diffusion. The model incorporates both short-range, steric and long-range, substrate-mediated elastic interactions between cells and is detailed in the *Materials and Methods*.

The ubiquitous traction force pattern generated by a single polarized cell with a long axis **a** and exerting a typical force **F** at its adhesions can be modeled as a force dipole, $P_{ij} = F_i a_j$ (Fig. 1*C*). Note that the cell traction forces are generated by actomyosin units within the cell, each of which acts as a force dipole. Therefore, the disks in our model simulations could represent parts of a cell, and their motion represents the dynamics of cell protrusions. The resulting deformation induced by a force dipole in the elastic substrate is given by the strain, u_{ij}, which is determined by a force balance in linear elastic theory (*SI Appendix*, section A), and depends on the material properties of the elastic medium, specifically, the stiffness or Young's modulus E, and the compressibility, given by the Poisson's ratio ν (48). The substrate deformation (u_{xx} component of strain) generated by a dipole (oriented along the laboratory x-axis) embedded on the surface of a linear elastic medium is shown in Fig. 1*D* for two representative values of ν. Here, the blue (red) coloring represents expanded (compressed) regions of the substrate. We note that the extracellular matrix in biological tissue is typically viscoelastic, and over long times, the cell-generated strains may relax. However, our model still applies at short time scales and for linearly elastic synthetic substrates such as polyacrylamide that are routinely used in cell culture experiments (19).

A second contractile force dipole will tend to position itself in and align its axis along the local principal stretch in the medium to reduce the substrate deformation. The resulting interaction potential arises from the minimal coupling of one dipole (denoted by β) with the medium strain induced by the other (denoted by α) and is given by $W^{\alpha\beta} = P^{\beta}_{ij} u^{\alpha}_{ij}$ (17). The interaction energy between two dipoles then decays with their separation distance as $W^{\alpha\beta} \sim (P^2/E) \cdot r^{-3}_{\alpha\beta}$. We denote the characteristic elastic interaction energy when the dipoles are separated by only one cell length as, $\mathcal{E}_c = P^2/(16Ed^3)$, where the detailed expression is derived in *SI Appendix*, section A. This coarse-grained description abstracts out the biophysical details of mechanotransduction but provides a simple physical model for the cell response to deformations in their elastic medium (18).

Representative simulation snapshots (Fig. 1*E*) of final configurations show that elastic dipolar interactions induce network formation in a stiffness-dependent manner. The *Central* snapshot corresponds to an optimal substrate stiffness E^* at which elastic interactions are maximal, while those to the *Left* (*Right*) correspond to substrates that are too soft (stiff) for connected network formation. The origin of this optimal stiffness lies in the adaptation of cell contractile forces to their substrate stiffness, as we discuss later.

Elastic Dipolar Interactions between Model Cells Induce Network Formation. We expect the multicellular structures resulting from the dipolar cell–cell interactions to depend on three crucial nondimensional combinations of model parameters: the ratio of a characteristic elastic interaction energy $\mathcal{E}_c$, to noise – denoted by $A = \mathcal{E}_c/k_B T_{\text{eff}}$ – the effective elastic interaction parameter; the number of cells N, equivalently expressed as a cell density or packing fraction, $\phi = \frac{\pi N d^2}{4L^2}$; and Poisson's ratio, ν, which determines the favorable configurations (both position and orientation) of a pair of dipoles. To show the types of multicellular structures that result from our model elastic interactions, we perform Brownian dynamics simulations (detailed in *Materials and Methods*) to generate representative snapshots at slices of this $A - \phi$ parameter space for two values of ν: 0.5 and 0.1, shown in Fig. 2 and *SI Appendix*, Fig. S4, respectively. As packing fraction is increased, networks form more readily. As the effective elastic interaction is increased, cells form into networks characterized by chains, junctions, and rings. This can be thought of naturally as a competition between entropy and energy. At low packing fractions or effective elastic interaction, cells are either in a gas-like state or form local chain segments with many open ends which have high entropy. As packing fraction or effective elastic interaction increases, cells relinquish translational and rotational freedom for more energetically favorable states such as longer chains, junctions, or rings. This is consistent with the cell density–dependent morphologies seen in images from in vitro hydrogel experiments (reproduced from ref. 43) and shown in Fig. 2.

We choose two representative values of ν in our model simulations because their corresponding strain plots are qualitatively different (37) as seen in Fig. 1*D*. Briefly, since contractile dipoles prefer to be on stretched regions of the substrate, the low (high) ν deformation patterns are expected to favor two (four) nearest neighbors. The different values of the Poisson ratio could correspond to synthetic hydrogel substrates and the fibrous extracellular matrix, respectively. While hydrogel substrates are nearly incompressible ($\nu = 0.5$), the ECM comprises of networks of fibers which permit remodeling and poroelastic flows leading to reduced material compressibility (e.g., $\nu = 0.1$) at long time scales (49).

Substrate Deformation–Mediated Interactions Strongly Enhance Percolation in Model Networks. To characterize the extent of multicellular network formation, we consider the percolation order parameter which quantifies the ability of a connected network to span the available space. Percolation is defined as the probability that, for a steady state realization of the network, there exists a continuous path through it that spans the length of the simulation box. To compute percolation probability, we first identify connected clusters of cells, a process detailed in *SI Appendix*, section E. A specific network configuration is considered to be percolating if any two cells within the same cluster are separated by a Euclidean distance greater than or equal to the simulation box size. The average values and corresponding errors are then plotted against varying packing fraction ϕ in Fig. 3*A* and varying effective elastic interaction parameter A in Fig. 3*B*. Multiple such simulations are then combined into a phase diagram in $A - \phi$ parameter space in Fig 3*C*. The results show that percolation requires both density and interaction strength to be above corresponding threshold values.

To contrast with the dipoles that mutually align through long-range and anisotropic interactions, we consider a control system of "diffusing sticky disks." These agents just diffuse without any long-range interactions and cease movement upon contact with another agent. We find percolating networks for both interacting elastic dipoles and diffusing sticky disks. However, Fig. 3*A* shows that model cells which interact as dipoles at long-range require far fewer cells to percolate than their sticky disk counterparts given that the elastic interaction strength is sufficiently greater than noise as shown in Fig. 3*B* ($A \gtrapprox 1$ in the case shown where $N = 300$). This is because the anisotropic nature of the dipolar interactions promotes end-to-end alignment of cells, creating elongated structures like chains, which can self-

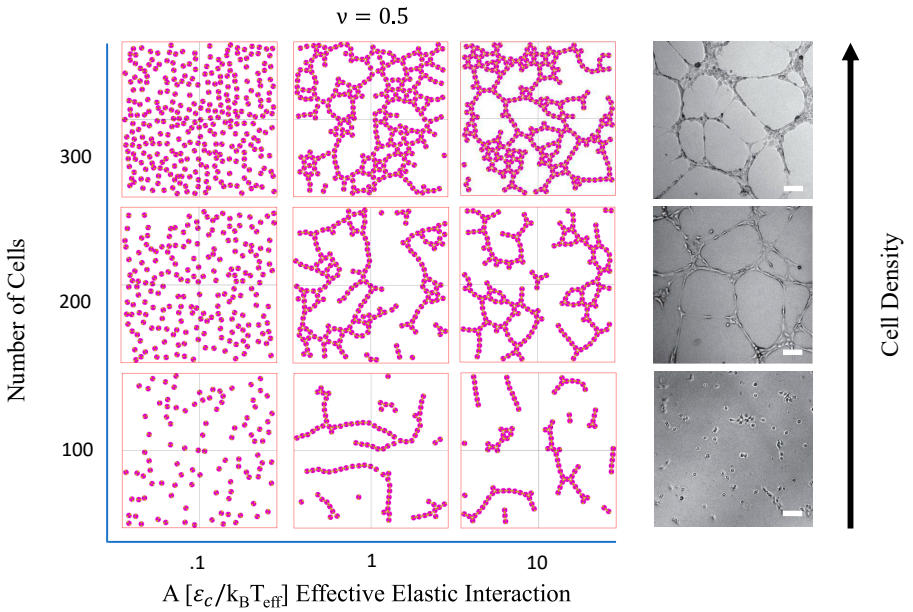

Fig. 2. Simulation snapshots showing representative final configurations of model cell dipoles. We explore the parameter space of number of cells and $A \equiv \frac{\varepsilon_c}{k_B T_{\text{eff}}}$, the ratio of the characteristic elastic interaction strength and noise, for Poisson's ratio, $\nu = 0.5$. At lower packing fractions, cells form disconnected linear clusters. At lower (A) values, cells remain isolated, but at moderate values of A and sufficient packing fraction, cells form space-spanning network configurations characterized by rings, branches, and junctions. At higher packing fractions, clumpy structures such as what previous literature calls "4-rings" occur frequently (38). The tendency for cells to form only local connections at low packing fraction and form space-spanning structures at higher packing fraction is consistent with experimental images of endothelial cells cultured on hydrogel substrates (*Right* column; images reprinted with permission from ref. 43) (Scale bars, 100 μm).

assemble into space-spanning networks. We therefore show that network formation requires fewer cells when cells can sense, move, and align in response to the substrate deformations created by other cells. Thus, networks guided by mechanical interactions are more cost efficient than when cells move or spread randomly, forming adhesive contacts upon finding their neighbors.

Much work has been done on characterizing the connectivity percolation transition on various lattice configurations (50). The critical packing fraction can be widely different depending on the lattice geometry and whether the space-spanning clusters comprise sites or bonds (51, 52). The critical packing fraction for site percolation is known to be $\phi_C = 0.5$ for an infinitely large triangular lattice (53). In approximate agreement with this, we find that the critical packing fraction for diffusive sticky disks for the current finite system size L is $\phi_C \approx 0.6$. For the dipolar particles, anisotropic interactions shift the percolation transition to $\phi_C \approx 0.2$, similar to those seen in dipolar colloidal assemblies at low reduced temperature (54).

Our observed packing fractions for transition to percolation are specific to the simulation system size, L, and differ from the actual critical packing fraction due to finite size effects. How prominent these effects will be depends on the fractal dimension, which provides a measure of how these structures scale with size. Since area scales like L^2, but number of particles scales like L^{d_f}, where d_f is the fractal dimension, $\phi_C \propto L^{d_f-2}$. Therefore, there exists a regime in which ϕ_C will decrease with increasing L, as shown by simulations with bigger box sizes (*SI Appendix*, section F). We present an analysis of the fractal dimension of these networks and corresponding experiments in the next section.

Analysis of Experimental Cell Cultures Confirms Predicted Substrate Stiffness Dependence of Cell Network Formation. We showed in the previous section that the cells' ability to form networks is expected to depend on the strength of elastic interactions arising from their mutual deformations of the substrate. To compare with experiments, we now consider how this elastic interaction strength A depends on the substrate stiffness. Experiments show that cells spread and polarize more on substrates of increasing stiffness, such that their traction force saturates to a maximal value P_0 at a characteristic substrate stiffness, E^*, that depends on cell type and matrix mechanochemistry. The effective elastic interaction parameter, A, can be mapped to substrate stiffness, E, by using a model relation predicting the dependence of cell traction force on substrate stiffness (55): $P = P_0 E/(E + E^*)$. The resulting elastic interaction parameter, A, is weak on softer substrates where cell forces are low and also on stiffer substrates, where the deformations are low. It reaches a maximum at the characteristic stiffness E^* as detailed in *SI Appendix*, section G. This mapping from effective elastic interaction to substrate stiffness (*SI Appendix*, Fig. S6) results in a peak in the percolation curves (*SI Appendix*, Figs. S8 *A* and *C*) over an interval of substrate stiffness centered around the optimal stiffness E^*. This interval depends on both cell density and effective temperature representing noisy cell movements. Higher effective temperature and lower cell density reduce both peak height and width. This result is consistent with experiments on EC cultures (Fig. 1*A*) which show that percolating networks form only in a certain range of substrate stiffness, but these previous works do not demonstrate that network formation is optimal at intermediate substrate stiffness (43, 44).

To test this prediction of our model, we performed 2D cell culture experiments on elastic substrates over a wide range of stiffness values. Human umbilical vascular endothelial cells (HUVECs) were cultured at three different seeding densities (8×10^3/cm^2, 14×10^3/cm^2, and 20×10^3/cm^2) on fibronectin-coated polyacrylamide substrates of varying stiffness: (200 Pa, 480 Pa, 1 kPa, 2 kPa, 4.5 kPa, and 10 kPa). The substrate preparation protocol, described in *Materials and Methods*, and stiffness characterization of these substrates follow standard

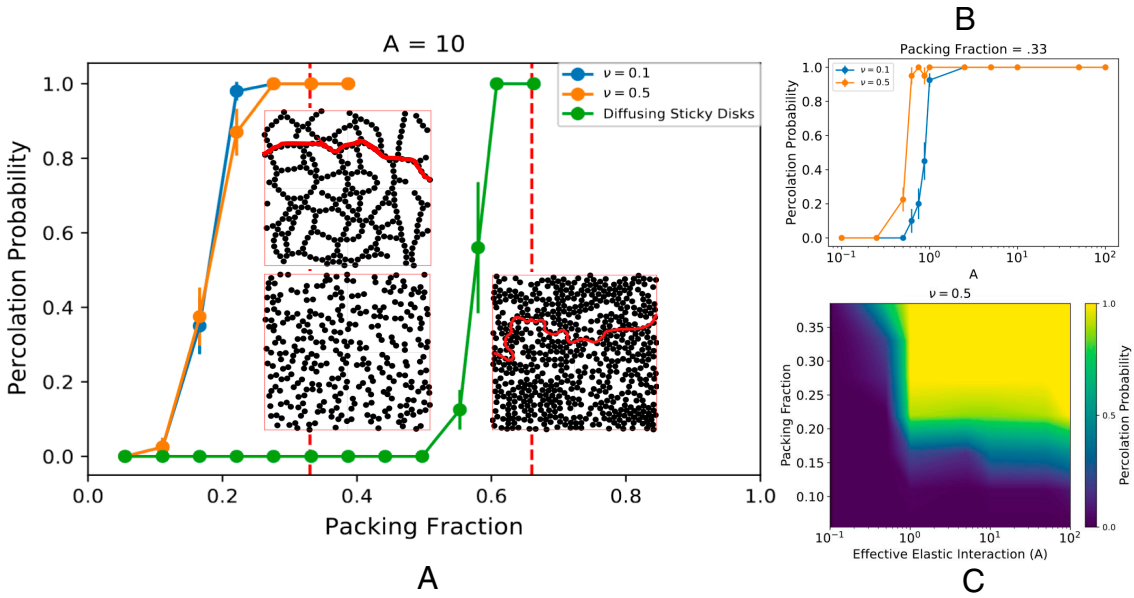

Fig. 3. Analysis of connectivity percolation of simulated cell clusters predicts dependence on cell density and strength of substrate-mediated elastic interactions. (*A*) Percolation probability for elastic dipoles—blue and orange —and diffusing sticky disks—green—as a function of area packing fraction, ϕ. Elastic dipoles undergo the percolation transition at lower packing fractions than purely diffusive, sticky disks. The insets show characteristic final configurations for both elastic dipoles and sticky disks at a packing fraction of 0.33($N = 300$), with an example percolating path shown in red. (*B*) The percolation probability for given packing fraction also exhibits a sharp transition in effective elastic interaction, (*A*). (*C*) Percolation phase diagram in packing fraction and effective elastic interaction space. Generally, network assembly is more likely for higher cell density and elastic interactions. Each data point and error bar represents the average and SEM, respectively, of forty simulations with the exception of sticky disks in (*A*) at the three largest packing fractions which represent nine simulations each, and A = 0.25, 0.625, 0.75, 0.875, and 2.5 in (*B*) which represent twenty simulations each.

precedents (56). Cells were fluorescently labeled and imaged at regular intervals over the course of 19 h post-seeding. While for the lower seeding density, network formation could be observed at these longer time scales (Fig. 4 *A*, *Middle*), the higher seeding density led to denser, isotropic clusters, and a resulting loss of network morphology (Fig. 4 *A*, *Right*). We then considered the images of these denser cultures at 9 h instead of 19 h, where network morphology was still apparent. We also observed that the dense isotropic clusters were more prevalent at higher substrate stiffness due to enhanced cell spreading and possibly proliferation at later times.

To quantitatively obtain the percolation probability for the observed cell clusters, we process the experimental images (Fig. 4*A*) by emphasizing intercellular connections as described in *Materials and Methods* under *Image Analysis*. We then parse the resulting binary images (Fig. 4*B*) into $N_B = 312$ subboxes each so as to obtain sufficient statistics from a single experimental image. We next computed the mean percolation probability over all subboxes, $p = \frac{1}{N_B}\sum_{i=1}^{N_B} p_i$ and the corresponding standard error of mean. Here, we set $p_i = 1$ if the ith subbox is "percolating," i.e., it contains a cluster that spans the subbox, and set $p_i = 0$ otherwise. To compare the sparser, heterogeneous experimental configurations with our simulated networks, we normalized these values by the maximum mean percolation probability across all experimental seeding densities and stiffnesses. For practical convenience, we henceforth denote the normalized percolation probability value as p.

We find that for both the lowest seeding density sampled at long times (Fig. 4 *C*, *Left*) and for the highest seeding density sampled at short times (Fig. 4 *C*, *Right*), the normalized experimental percolation probability exhibits a peak at a stiffness of about 4.5 kPa. Unlike simulations where packing fraction and elastic interaction are independent parameters, the area covered by cells in experiments depends on stiffness because cells spread more on stiffer substrates. This is why we need a range of packing fraction values from simulation to compare with experiment. Like the experimental images, the simulation images were skeletonized to emphasize inter-particle connections (*Materials and Methods* and *Image Analysis*). We denote the corresponding packing fraction of skeletonized images by $\tilde{\phi}$ to distinguish from the packing fraction of simulated disks, ϕ. We then plot a family of interpolated simulation curves as a function of substrate stiffness over a range of packing fraction values, $\tilde{\phi}$, chosen to fit the experimental data in Fig. 4*C*. These values are close to the range of packing fraction values in experimental images (0.05 to 0.15 for $\frac{8k}{\text{cm}^2}$ and 0.1 to 0.2 for $\frac{20k}{\text{cm}^2}$). The quantitative agreement of the experimental data with simulation values lends credence to our model that network formation is driven by substrate-mediated elastic interactions and that these are stronger within a range of substrate stiffness values centered around an optimal value, E^*.

We note an important distinction between the predictions of the cell dipole model and the observed cell clusters in experiments. These latter tend to exhibit isotropic dense clusters on stiffer substrates at higher seeding density. We expect this is because cells spread more on stiffer substrates and form direct adhesive contacts with neighbors. Cell spreading and direct cell–cell contact-based interactions are not implemented in our minimal model since we focus on the long-range substrate-mediated dipolar interactions expected to dominate in dilute cultures. At higher densities, endothelial cells are known to form confluent monolayers (57). At intermediate densities, some of these dense isotropic clusters occur alongside networks and elongated structures. Modeling these would require a combination of cell–cell and cell–substrate forces. Although dense isotropic clusters are not seen in our dipole simulations (Fig. 1*E*), their occurrence in experiment supports our model expectation that the dipolar elastic interaction strength (A) becomes smaller on

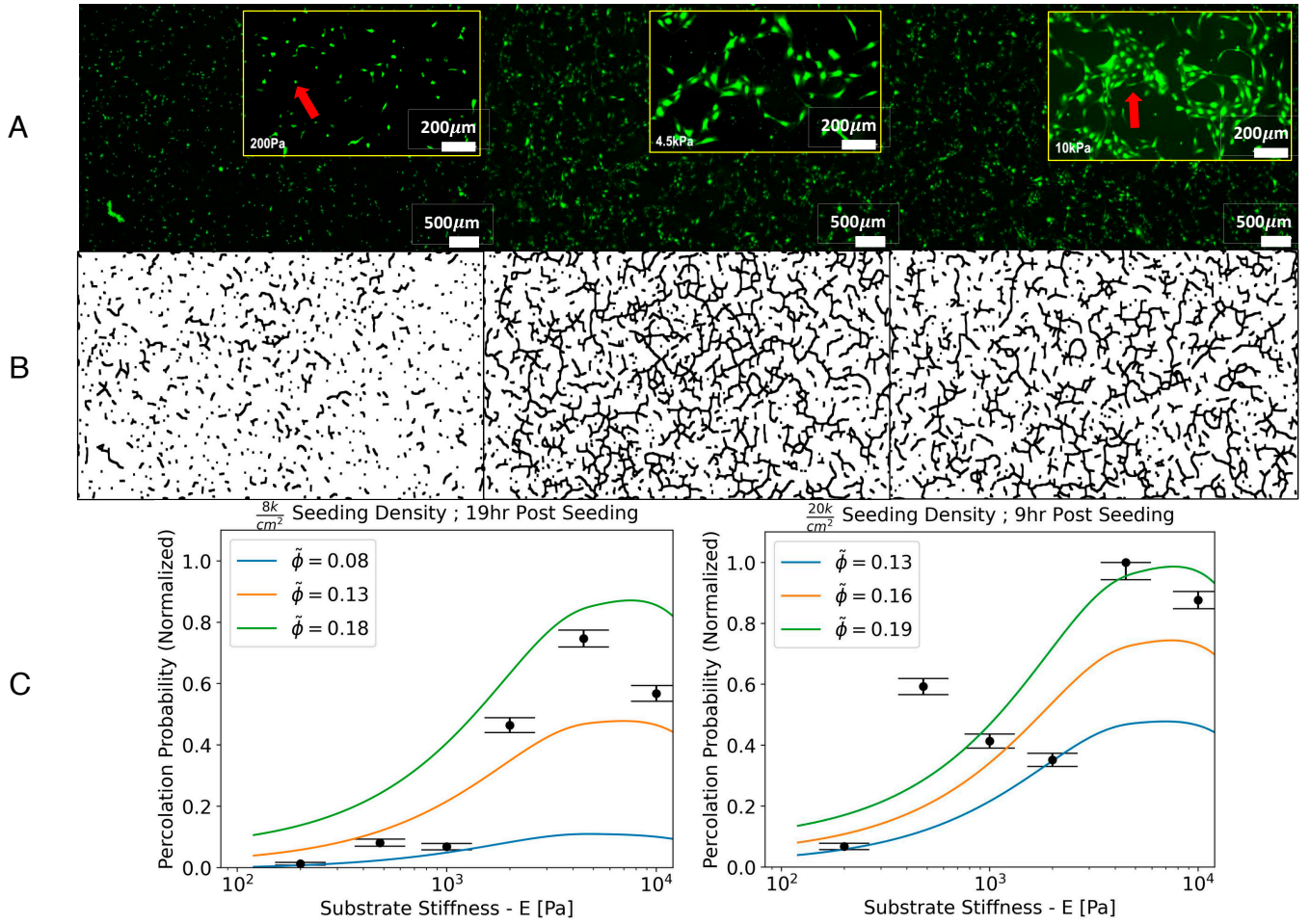

Fig. 4. Analysis of connected clusters of endothelial cells cultured on elastic substrates reveals optimal stiffness for cell network formation (*A*) Experimental images of human umbilical vascular endothelial cells (HUVECs) at $8 \times 10^3/\text{cm}^2$ seeding density 19 h post seeding on polyacrylamide substrates of varying stiffness: 200 kPa (*Left*), 4.5 kPa (*Middle*), and 10 kPa (*Right*). Insets show 10× magnified images of the full field of view. Cells on substrates of lower stiffness tend to remain largely isotropic and isolated (shown by a red arrow on the *Left*) and do not form intercellular connections. Cells on substrates of higher stiffness tend to spread and aggregate into dense isotropic clusters (shown by the red arrow on the *Right*). Both these tendencies counteract efficient network assembly. (*B*) Processed binary skeletons of the raw images in (*A*). Qualitatively, the intermediate substrate stiffness exhibits the most prominent networks. (*C*) Quantitative measurement of the percolation probability from experimental images such as shown in (*B*) supports the model prediction that network formation is optimal on substrates of intermediate stiffness. *Left* and *Right* plots show normalized percolation probability values measured for two different initial cell seeding densities, $8 \times 10^3/\text{cm}^2$ and $20 \times 10^3/\text{cm}^2$, respectively. The higher density cell culture data (*Right*) are selected at an earlier time (9 h post seeding) because these cells form dense isotropic clusters at later times. The continuous curves represent model predictions for percolation probability as a function of substrate stiffness at three different representative values of the packing fraction from skeletonized simulation images, $\tilde{\phi}$. These are chosen to approximately correspond to the experimental packing fraction, which however varies with substrate stiffness due to cell spreading. Percolation curves from simulation in (*C*) were interpolated from average values obtained for forty simulations. Experimental data points and error bars are average and SEM, respectively, of subboxes as described in *Materials and Methods*.

stiffer substrates in relation to the isotropic, cell–cell contact interactions.

While the percolation analysis shown in Fig. 4 validated our model predictions for the substrate stiffness–dependence of network formation, we now seek to predict characteristic morphological traits of the cell clusters. A careful examination of experimental images in Figs. 4 and 5 reveals distinct morphologies of cell clusters, ranging from isolated cells and isotropic clusters to networks and elongated clusters. To obtain a measure of how elongated each cell cluster is, we calculate a "shape parameter," defined as $s \equiv \frac{R_g^2}{Area} = \frac{1}{N^2}\sum_{k=1}^{N}(\mathbf{r}_k - \mathbf{r}_{CM})^2$, for each unique cluster as described in *Materials and Methods* under *Image Analysis*. Here, R_g represents the radius of gyration of the cluster, which is defined about its center-of-mass $\mathbf{r}_{CM}$, and N is the number of occupied pixels in each cluster. The normalization by cluster area ensures that we control for cluster size variations between different experiments. Lower values of this shape parameter correspond to isotropic shapes, the theoretical lower bound being $\frac{1}{2\pi}$ for a solid circular disk. Conversely, a higher shape parameter corresponds to more elongated clusters. To compare with simulation, we scale the shape parameter of each cluster by their global mean across all identified clusters at the different seeding densities and stiffnesses. Henceforth, the scaled values of the shape parameter are denoted by s.

To classify the dominant morphological feature in each image, we constructed a composite order parameter combining the global information of connectivity percolation with the local cluster-scale morphological characteristics captured by the shape factor. The order parameter is defined such that clusters with normalized percolation probability above a threshold value ($p_T = 0.7$) are considered "networks." We choose this value of p_T to pick out experimental images where a few of the largest clusters contain more than 20% of the total filled area (*SI Appendix*, Fig. S20). If $p < p_T$, implying that there are no dominant space-

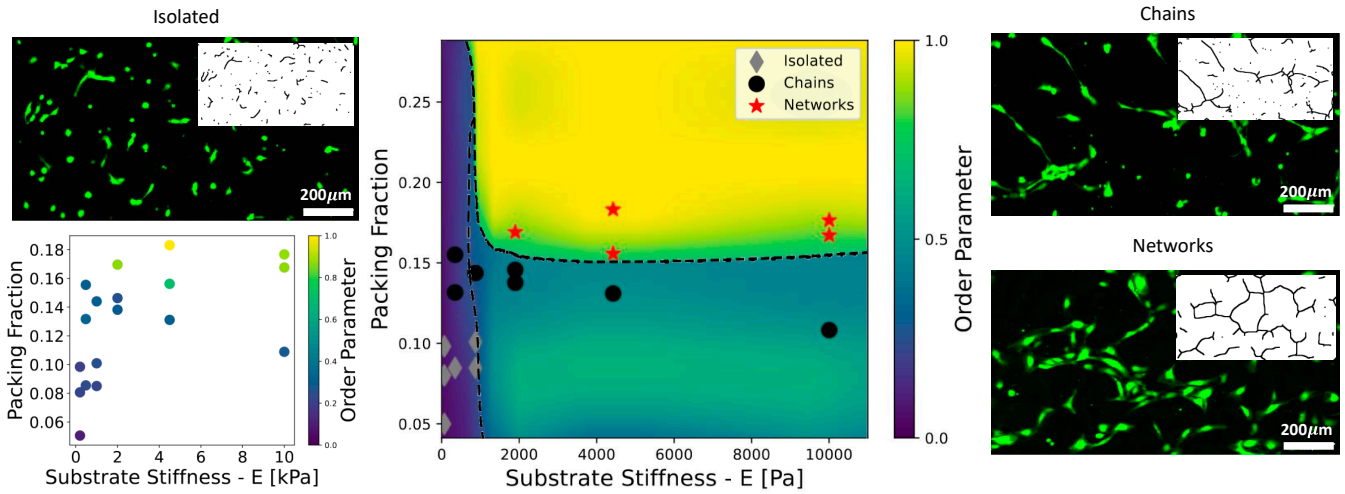

Fig. 5. Experiments validate predicted classification of cell cluster morphology into distinct phases. (*Center*) "Phase diagram" of the distinct morphology of cell clusters, based on cell density and substrate stiffness. The color map represents a composite order parameter (*OP*, detailed definition in the text) designed to capture both the cluster percolation probability *p* and the cluster shape parameter *s* as a single value. Ranges of the order parameter values $OP > 0.7$, 0.25 to 0.7, and < 0.25 correspond to percolating "networks," elongated but disconnected "chains," and isotropic "isolated" clusters, respectively. The background color map is created by interpolating over a set of order parameter values obtained from simulations of varying cell number (plotted as $\tilde{\phi}$ - the postskeletonized filling fraction) and elastic interaction strength. The experimental data points, corresponding to different cell densities (measured as fractional area covered by cells in microscopy images) and substrate stiffness, are classified according to the measured value of the order parameter and overlaid on the simulated phase diagram. They demonstrate good agreement with the predicted phase boundaries (dashed lines). At the *Left Bottom* is the phase diagram showing the experimental order parameter values using the same color map as the simulation results in the central phase diagram. This reveals the nonmonotonic behavior of the order parameter vs. substrate stiffness for the percolating networks, confirming the results of Fig. 4*C*. *Left-Top*, *Right-Top*, and *Right-Bottom*, Representative images from the cell culture experiments (at highest seeding density) and corresponding skeletonized images, to illustrate the occurrence of isolated cells, elongated chains, and percolating networks for substrates of stiffness, 200 Pa, 480 Pa, and 4.5 kPa, respectively. Simulation values used to construct the colormap in the center panel are averaged over forty simulations for percolation and three simulations for shape factor for each data point.

spanning clusters, we classify clusters into "isolated" or "chains," depending on whether s is less or greater than a threshold value $s_T = 0.95$. This value of s_T is chosen to correspond to simulations with two aligned dipoles, giving an elongated morphology that this parameter is designed to capture. The order parameter which accomplishes the above classification is given by $\mathrm{OP} \equiv \Theta(p - p_T)p + \Theta(p_T - p)(0.25 + 0.5(s - s_T))$, where $\Theta(x)$ is the Heaviside step function and the numerical factors give an $0 < OP < 1$ for the specific values of s_T and p_T, justified above. The differences are captured by ranges of values of the order parameter: $OP > 0.7$, 0.25 to 0.7, and < 0.25 correspond to percolating "networks," elongated but disconnected "chains," and isotropic "isolated" clusters, respectively.

We compute this order parameter for interpolated simulation data and for experimental data 9 h post seeding, so that cell proliferation effects are minimal. Experimental data once again reveal a nonmonotonicity in network formation at the high densities in Fig. 5, *Bottom Left*. We construct a phase diagram of this order parameter in $\tilde{\phi} - E$ space (Fig. 5, *Center*), where the color map corresponds to simulation data. Overlaid on this phase diagram are discrete markers representing experimental data, which have been classified into the three distinct regimes according to their measured order parameter values. The data comprise three initial seeding densities and six stiffness values giving a total of eighteen data points. Their distribution clearly shows a correlation between cell area coverage and substrate stiffness. This is due to cells spreading more on stiffer substrates, readily seen through the lack of low packing fraction data at higher stiffness.

Phase boundaries are drawn as dashed lines that delineate the distinct regions of the simulation order parameter values. Of the eighteen experimental data points, only two lie outside of the corresponding predicted regions. Both of these are at low substrate stiffness and intermediate packing fraction. These are classified as "chains," but lie in the "isolated" part of the predicted phase diagram. We expect that at these intermediate densities, cells can spread and touch each other to form elongated structures even if the elastic dipolar interactions are small. Since our model does not include such spreading effects, this discrepancy is not surprising. Overall, the model phase diagram closely predicts the experimentally observed multicellular structures.

We now further evaluate the morphological similarity of the networks from our simulated dipoles and our experimental cell culture by calculating the fractal dimension. For the "sticky disks," we find a fractal dimension of $d_f = 1.81$, whereas for the dipoles, we find fractal dimensions of $d_f = 1.698 \pm 0.004$ and $d_f = 1.711 \pm 0.003$ for $\nu = 0.1$ and $\nu = 0.5$, respectively. We find a similar fractal dimension for our experimental HUVEC culture in the network regime on a substrate of stiffness $E = 4.5$ kPa, $d_f = 1.722$. Interestingly, simulated networks on substrates of $\nu = 0.1$ and $\nu = 0.5$ are statistically distinguishable, with the experimental fractal dimension showing reasonable agreement with the $\nu = 0.5$ simulated dipole case. This is in accordance with the approximately incompressible nature of hydrogel substrates. The proximity of the fractal dimensions of the simulated dipoles to that of experimental cell networks, in relation to the sticky disks, indicates that cells utilize a more complex strategy to self-assemble than simply random movement followed by cell–cell adhesion. The elastic dipolar interactions are thus a plausible strategy allowing the self-assembly of biologically desirable, space-spanning, and cost-effective networks.

Diverse Poisson-Ratio Dependent Morphological Features Offer Distinct Advantages in Network Assembly and Transport Function. We now focus on simulated networks (such as in Fig. 3) to thoroughly characterize their two predominant network morphological constituents—branches and rings. We relate the resulting structural metrics to the transport function of biological

networks. We highlight qualitative differences in morphology of simulated networks between elastic substrates with high and low Poisson's ratio values, which may motivate future experimental investigation. Fig. 6*A* shows average branch length for $N = 300$ ($\phi = 0.33$) cells as a function of effective elastic interaction (A). The average branch length for the higher ν case remains roughly constant and low at about two cell lengths. The lower ν case exhibits a peak in average branch length at the percolation threshold ($A = 1$) before decreasing and saturating at high A values. The distribution of branch lengths (Fig. 6*B*) shows that while $\nu = 0.5$ is sharply peaked at d, $\nu = 0.1$ exhibits branches greater than 18 d and shows a greater relative count in the 3 to 10 d range.

These results suggest that at higher values of ν, network morphology is more resilient to noise, and the branch lengths are not as easily tunable, The greater variability in branch lengths leads to longer branches in the lower $\nu = 0.1$ case, which then requires (for $A \geq 5$) fewer cells to percolate than at $\nu = 0.5$. This is seen by the difference of the curves at the shoulder of the percolation transition in Fig. 3*A* and *SI Appendix*, Fig. S10. The greater resilience of the network at higher substrate ν leads to percolation at smaller A than its low ν counterpart (Fig. 3*B* and *SI Appendix*, Fig. S10). In *SI Appendix*, section I, we construct a detailed map of the percolation transition in the $A-\phi$ parameter space, to show how $\nu = 0.1$ requires fewer cells to percolate for a range of A values, while $\nu = 0.5$ can percolate at lower values of A. This suggests that the two regimes of substrate compressibility optimize two different measures of cost of network building: one, the number of cells, and the other, the strength of cell contractility.

Fig. 6*C* shows a cumulative distribution of ring area for our networks at two crucial regions in our parameter space—those at which the networks are well above the percolation transition (solid lines), or just above it (dashed lines). Similar to the branch length distribution, the networks at higher ν form many small rings and few large rings, while the lower ν case shows a broader distribution of ring sizes. The tendency of the

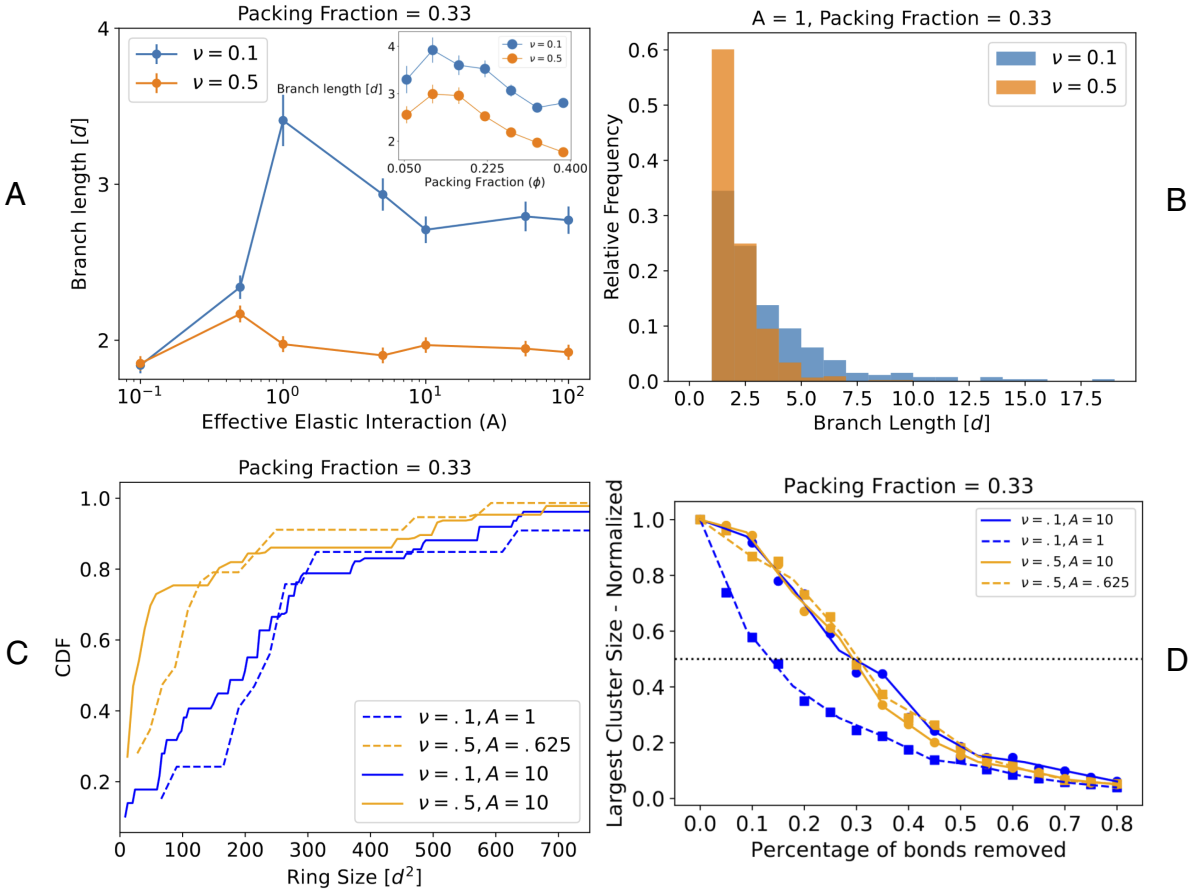

Fig. 6. Substrate compressibility and rigidity affect efficiency and resilience of model networks. (*A*) Average branch length as a function of the effective elastic interaction for $N = 300(\phi \approx 0.33)$ cells. The lower ν case shows a greater sensitivity to A indicating a greater aptitude for tunability than the high ν counterpart. The inset shows average branch length as a function of packing fraction when $A = 10$. Both values of ν show similar behavior except at the highest point of packing fraction. At this packing fraction, the curves diverge as global configurations begin to become prevalent. For the low ν case, this will be long parallel strings, whereas the high ν case will form a single cluster of 4-rings. (*B*) Normalized branch length histogram for $A = 1$ and $\phi = 0.33$. The networks on substrates of high ν are sharply peaked around the smallest branch lengths while the networks at low ν exhibit a broader, longer-tailed distribution. (*C*) Cumulative distribution of ring area for $N = 300(\phi \approx 0.33)$ cells shown both for networks at the shoulder of the percolation transition and networks well beyond the transition. Networks at high ν contain smaller rings than the networks at low ν. Irreversible networks show more smaller rings as noise is not great enough to jostle these compact structures apart to favor more stringy morphologies. (*D*) Largest cluster size as a function of the fraction of network branch segments removed—a measure of a network's ability to to maintain functionality after being damaged (49). Networks at the shoulder of the percolation transition exhibit less robustness than those well above the percolation transition for the $\nu = 0.1$ case. In the $\nu = 0.5$ case, however, networks retain their robustness even at the shoulder of the percolation transition. As this robustness metric saturates at a value of A dependent on the compressibility of the substrate, we hypothesize cells interacting in the way that we have estimated will tend to exert only a certain amount of force, enough to build a resilient network and no more. Each data point and error bar in (*A* and *B*) represent the average and SEM, respectively, of three representative simulations. Data points in (*C*) are for a representative dipole configuration per parameter value. Data points in (*D*) are averages of 20 trials per percentage of bonds.

$\nu = 0.5$ configurations to form numerous smaller rings leads to a marginally less efficient area coverage than the low ν case, which forms longer branches and fewer small rings (*SI Appendix*, Fig. S11). These results are also consistent with the fractal dimensions we obtained earlier, with d_f being slightly higher for the $\nu = 0.5$ than the 0.1 cases, indicating more compact structures for the former. These topological features also give rise to distinct coordination numbers for the two compressibility regimes (*SI Appendix*, Fig. S18). Interestingly, the coordination number on the lower Poisson ratio substrate resembles those near the rigidity percolation of elastic fiber networks (58, 59)—indicating connectivity percolation as a precursor to mechanical rigidity which is relevant to both tissue development and disease (60).

To examine the robustness of our model networks to damage, a biologically significant property, we measure the largest remaining cluster size as a function of the fraction of network bonds removed (61) (Fig. 6*D*). We find that whether well above or just at the percolation threshold, the networks at higher ν retain cluster size well as bonds are removed. Networks at lower ν well above the percolation transition lose largest cluster size at the same rate as their higher ν counterpart. At the shoulder of percolation, however, networks at low ν lose largest cluster size and fall apart much more rapidly than any of the other networks. This is the same parameter regime at which networks at low ν exhibit a peak in branch length. By forming long branches, ring structure formation is sacrificed. Thus, we find that the prime factor for robust networks is the tendency to form rings which provide degeneracy to paths between any two nodes in the network—a result consistent with network structure optimization models (62). In summary, at lower ν, networks tend to form longer and more broadly distributed branches which promote efficiency with respect to the filling and spanning of space at the cost of being susceptible to damage, while at higher ν, networks are predominantly composed of small rings, which provide robustness to the networks at the cost of transport efficiency.

Discussion

Our model generates testable predictions for the dependence of cell network morphology on substrate mechanical properties. By performing and analyzing experiments on ECs cultured on hydrogels of varying stiffness, we show that network formation is indeed optimized at an intermediate stiffness. Although many experiments show that EC network formation or capillary sprouting requires softer matrices (ref. 63 and references therein), these findings can show different trends at different stiffness regimes (64, 65). We suggest that this may be because cells adapt their traction forces to substrate stiffness, and therefore, the expected optimal stiffness for network formation should be where cells attain their maximal contractility. This optimal stiffness may be dependent on cell type and matrix mechanochemistry (44).

Our modeling thus relates network structure to cell contractility, and the predictions can be further checked in cell culture experiments on substrates of varying stiffness and Poisson's ratio (49), that combine traction force measurement with quantification of network morphology. The presence of substrate deformation–mediated interactions can also be directly investigated in a two-cell setup on a micropatterned substrate which allows one to observe reorientations of one cell in response to the other, similar to strategies used to examine pairwise interactions during cell motility (66) and cardiomyocyte synchronization (25).

Further, cells may persistently migrate, in addition to the stochastic movements assumed in the present model. Our prior work suggests that cells form stable network structures rapidly at lower migration speeds (47). At high persistent migration speeds, the networks dissolve and the dipoles self-organize instead into motile chains. This suggests that an optimum cell migration speed is favorable for network formation, which cells may achieve through self-regulation of their motility through interaction with their neighbors, such as contact inhibition of locomotion.

A crucial modeling challenge for vasculogenesis, and other instances of cell network formation in biology, is that multiple factors ranging from cell differentiation to chemotactic cues could be involved in vivo. Modeling approaches based on different hypotheses can all lead to network pattern formation (67). Here, by combining experiments on hydrogels of varying stiffness and a physical model based on mechanical interactions alone, we aim to isolate the different factors involved. While we focus on endothelial cell networks as a model system, our predictions are generally applicable to other contractile cell types that self-organize into networks such as fibroblasts (68), neurons, or smooth muscle cells (*SI Appendix*, Table S1), as well as to synthetic particles with electric or magnetic dipolar interactions, that are of interest in materials science. In summary, our work provides proof-of-concept that substrate-mediated elastic interactions are a physical strategy that biological cells may employ to direct their self-organization into efficiently space-spanning, multicellular networks.

Materials and Methods

A. Model Details. We model the ubiquitous traction force pattern of a polarized cell as a single, anisotropic force dipole. The dipole magnitude is the cell force times the distance along the long axis of the cell, $P = Fa$. Since the contractile cytoskeletal machinery (e.g., actomyosin stress fibers) of the cell is typically aligned along this axis, this is also usually the principal direction of stress exerted by the cell and is henceforth called the "dipole axis." Such a force dipole induces a strain in the substrate, which is modeled as an infinitely thick, linear, isotropic elastic medium.

By considering two dipoles $\mathbf{P}^\alpha$ and $\mathbf{P}^\beta$, we show in *SI Appendix*, section A that the work done by a dipole β in deforming the elastic medium in the presence of the strain created by the other dipole α is given by (37): $W^{\alpha\beta} = P^\beta_{il} u^\alpha_{il}(\mathbf{r}^\beta)$, where the strain can be written in terms of $\mathbf{P}^\alpha$ and second derivatives of an elastic Green's function as $u^\alpha_{il}(\mathbf{r}^\beta) = \partial_l \partial_k G_{ij}(\mathbf{r}^\beta - \mathbf{r}^\alpha) P^\alpha_{jk}$. This minimal coupling between dipolar stress and medium strain represents the mechanical interaction energy between dipoles. Typical substrate strains are shown in Fig. 1*D*, where the blue (red) coloring represents expanded (compressed) regions. A second or test dipole present in these regions would tend to align its contractile axis along the principal stretch direction of the substrate. In the expanded (blue) regions, the test dipole is aligned with and attracted toward the central dipole, whereas in the compressed (red) regions, a test dipole is aligned orthogonal to and repelled away from the central dipole. The orientational dependence of the strain field is changed by the Poisson's ratio or compressibility of the substrate (18).

Our computational "many-cell" model considers cells as discrete agents (N agents in a $L \times L$ box with periodic boundary conditions) which move and orient randomly, but that also interact with one another through long-range elastic interactions via a force dipole strain field coupling and a short-range repulsive spring. Fig. 1*E* shows our simulation setup and the main ingredients of the model. We ignore details of the cell shape and subcellular structures in this minimal model and instead consider the cells as disk-shaped agents endowed with contractile, elastic dipoles. This simplifying assumption implies that we do not consider changes in the shape and size of individual cells that occur as a result of cell–substrate feedback when substrate stiffness is varied but instead focus on the multicellular structures at longer length scales.

We now consider the translational and orientational dynamics of a collection of model cells. These interact with each other through short-range, steric and long-range, substrate-mediated, elastic interactions, and undergo diffusive motion. The overdamped Langevin dynamics governing the position of a cell labeled α is

$$\frac{d\mathbf{r}_\alpha}{dt} = -\mu_T \sum_\beta \frac{\partial W_{\alpha\beta}}{\partial r_\alpha} + \sqrt{2D_\mathrm{T}}\ \boldsymbol{\eta}_{\alpha,\mathrm{T}}(t) \qquad [1]$$

where D_T is the effective translational diffusivity quantifying the random motion of an isolated moving cell, with $\boldsymbol{\eta}_\mathrm{T}$ as a random white noise term whose components satisfy $\langle \eta_{i,\mathrm{T}}(t)\eta_{j,\mathrm{T}}(t')\rangle = \delta(t-t')\delta_{ij}$. Typical adherent cells do not move very persistently, and at time scales much longer than their persistence time, their motion is random and has been shown to be well characterized by a diffusion constant (69). We thus neglect the directed self-propulsion term typically included for active particles from the dynamics. The mobility μ_T in Eq. **1** is inversely related to the effective friction from the medium that the moving cell experiences at its adhesive contacts with the substrate. Similarly, the orientational dynamics of the cell denoted by α is given by

$$\frac{d\hat{\mathbf{n}}_\alpha}{dt} = -\mu_R \sum_\beta \hat{\mathbf{n}}_\alpha \times \frac{\partial W_{\alpha\beta}}{\partial \hat{\mathbf{n}}_\alpha} + \sqrt{2D_\mathrm{R}}\ \boldsymbol{\eta}_{\alpha,\mathrm{R}}(t), \qquad [2]$$

where $\hat{\mathbf{n}}_\alpha$ is the unit vector along the dipole axis of the cell α and D_R is the effective rotational diffusivity quantifying the random reorientations of an isolated moving cell. Cells encounter various forms of internal stochastic effects including internal cytoskeletal rearrangements producing membrane morphological fluctuations, substrate surface binding fluctuations, and fluctuations in myosin motor forces, which are all absorbed into a coarse-grained effective temperature, T_eff, in our model. Single cell and cell cluster experiments have shown this effective temperature to be on the order of 10^{-15} to 10^{-14} J (70). Though the rotational and translational diffusion are in principle independent, we will here assume them to correspond to the same underlying processes and therefore the same effective temperature, $k_BT_\mathrm{eff} = D_T/\mu_T = D_R/\mu_R$. We also show some exceptions to this assumption in *SI Appendix*, section L, which all robustly form networks.

The pairwise cell–cell interaction potential $W_{\alpha\beta}$ between cells labeled α and β consists of the long-range elastic interaction arising through their mutual deformation of the substrate (*SI Appendix*, section A), and a short-range steric interaction between two cells in contact, and is given by,

$$\begin{aligned} W_{\alpha\beta} &= \frac{1}{2}k(d-r_{\alpha\beta})^2, \quad \text{when} \quad 0 \le r_{\alpha\beta} \le d \\ &= \frac{P^2}{E}\frac{f(\nu,\theta_\alpha,\theta_\beta)}{r_{\alpha\beta}^3}, \quad \text{when} \quad r_{\alpha\beta} > d, \end{aligned} \qquad [3]$$

where f is a function of Poisson's ratio–shown in *SI Appendix*, section A, θ_α, and θ_β where $\cos\theta_\alpha = \hat{\mathbf{n}}_\alpha \cdot \hat{\mathbf{r}}_{\alpha\beta}$ and $\cos\theta_\beta = \hat{\mathbf{n}}_\beta \cdot \hat{\mathbf{r}}_{\alpha\beta}$ are the orientations of cell α and cell β with respect to their separation vector, $\mathbf{r}_{\alpha\beta} = \mathbf{r}_\beta - \mathbf{r}_\alpha$ connecting the centers of the two model cell dipoles, respectively. Note that while the elastic potential is in principle long range, it decays strongly as a $1/r^3$ power law; we cut this pairwise interaction off at $r_{\alpha\beta} > 3d$ in our simulations, since the substrate strain induced by one cell is unlikely to be detected by a cell few cell lengths away (24).

The above equations are nondimensionalized by a suitable choice of length, time, and energy scales. By choosing the length scale to be the cell diameter d, the time scale to be an elastic time, $t_c = \frac{16Ed^5}{P^2\mu_\mathrm{T}}$, and a characteristic elastic interaction as the energy scale, $\mathcal{E}_c = \frac{P^2}{16Ed^3}$, the dynamical equations reduce to (Appendix B),

$$\frac{d\mathbf{r}^*_\alpha}{dt^*} = -\sum_\beta \frac{\partial W^*_{\alpha\beta}}{\partial r^*_\alpha} + \sqrt{\frac{2}{A}}\ \boldsymbol{\eta}^*_{\alpha,\mathrm{T}}(t^*), \qquad [4]$$

for the translational motion, while the rotational equation of motion can be written as

$$\frac{d\hat{\mathbf{n}}_\alpha}{dt^*} = -\sum_\beta \hat{\mathbf{n}}_\alpha \times \frac{\partial W^*_{\alpha\beta}}{\partial \hat{\mathbf{n}}_\alpha} + \sqrt{\frac{2}{A}}\ \boldsymbol{\eta}^*_{\alpha,\mathrm{R}}(t^*), \qquad [5]$$

where the starred variables indicate nondimensionalized quantities and we have assumed $\mu_\mathrm{R}d^2 = \mu_\mathrm{T}$ and $D_\mathrm{R}d^2 = D_\mathrm{T}$, although the latter is not required for a system that is out of equilibrium. The nondimensionalized pairwise interaction potential in Eq. **3** is here given by $W^*_{\alpha\beta} = \frac{1}{2}k^*(1-r^*)^2\Theta(1-r^*) - \frac{16f}{r^{*3}}\Theta(r^*-1)$, where $k^* = kd^2/\mathcal{E}_c$. We introduce an effective elastic interaction parameter quantifying the elastic interaction strength relative to that of intrinsic noise in the cell motion,

$$A = \frac{P^2\mu_T}{16Ed^3D_T} = \frac{\mathcal{E}_c}{k_BT_\mathrm{eff}}, \qquad [6]$$

where the noisy cell movements correspond to an effective temperature, $k_BT_\mathrm{eff} \equiv D_T/\mu_T$. This explicitly shows that A is a measure of the characteristic elastic interaction energy scale relative to the magnitude of cell stochasticity described by an effective temperature.

B. Physiological Estimates of Parameter Values. In experiments, the value of the effective interaction parameter A will depend on cell contractility, the stiffness of the elastic substrate, and the diffusivity that originates from the motility of single cells. Importantly, cells adapt their contractile forces to the stiffness of the underlying substrate. Measurements (71) and models (55) of the dependence of cell force on substrate stiffness suggest that the magnitude of the force dipole can be written as $P(E) = P_0/(1+E/E^*)$, where the characteristic substrate stiffness for a given cell at which the cell traction forces saturate to their maximal value is denoted by E^*. This dependence when inserted into the definition of the effective elastic interaction parameter, A, in Eq. **6**, leads to A being a peaked function of E. Since stiffer substrates are harder to deform and cells on softer substrates do not generate enough traction, substrate deformations and therefore elastic interactions are maximal at an intermediate optimal stiffness value ($E = E^*$) (Table 1).

To identify a plausible range for the values of A consistent with cell culture experiments, we note that the typical values for the force dipole for contractile cells adhered to elastic substrates is $P_0 = Fd \sim 10^{-12}$ to 10^{-11} J (31, 38). This corresponds to measured traction forces of $F \sim 10$ to 100 nN with a distance of $\sim$50 μm separating the adhesion sites at which the forces act on the substrate (29, 69), which is also the typical size of the cell along its long axis. For a typical substrate stiffness of $E \sim 1$ kPa characteristic of EC network formation (43, 44), we therefore estimate an elastic dipole energy of $\mathcal{E}_c = \frac{P^2}{16Ed^3} = \frac{F^2}{16Ed} \sim 10^{-15}$ J, similar to measured values for cell contractile energy stored in the elastic substrate (72). Since adherent cells crawl by exerting forces at the focal adhesions at which forces are transmitted to the substrate, the net mobility that determines cell translation, μ_T, can be estimated from the friction force at these adhesion sites. From the observation that the focal adhesions with surface area of 10 μm^2 reorient with speeds of μm/min in the direction of an external, applied stress of kPa (73), we can estimate the mobility coefficient (inverse of friction coefficient) to be $\mu_T \sim 0.1\ \mu\mathrm{m/min\ pN^{-1}}$. The effective diffusivity characterizing single endothelial cell movements was measured to be $\sim$10 μm^2/min (23, 43, 74). Together, these give an estimate for the effective temperature: $k_BT_\mathrm{eff} = D_T/\mu_T \sim 10^{-16}$ J $\sim 10^4\ k_BT$. For substrate stiffness

Table 1. Simulation parameters and their meaning

Parameter	Interpretation	Simulation values
A	Elastic interaction : Noise	0.1 to 100
k^*	Steric interaction	1.6×10^3
ϕ	Cell packing fraction	0.05 to 0.5
d	Cell diameter	1
L	Box size	26.66

$E \sim E^*$ 1 kPa, we thus estimate the ratio of elastic energy to noise to be $A = \mathcal{E}_c / k_B T_{\text{eff}} \sim 10$.

In experiments, the substrate stiffness can be tuned over a wide range. In particular, Califano et al. tested the formation of EC networks on substrates whose rigidity was varied from 100 Pa to 10 kPa (44). This, in our estimate, corresponds to an interaction parameter $A \sim 1 - 100$, with $A = 0.1$ corresponding to high noise or nonoptimal values of substrate stiffness (too soft or too stiff). Similarly, we can estimate the characteristic timescale as $t_c = \frac{d^2}{\mathcal{E}_c \mu_T} \sim 10^2$ min. This timescale of hours is consistent with that required for the formation of cellular structures in experiments (44).

C. Experimental Methods.

Cell culture. Green florescent protein (GFP)–expressing human umbilical vein endothelial cells (HUVECs) (Angio-Proteomie) were expanded on 10 mg/mL fibronectin-coated plates in Endothelial Cell Growth Medium-2 with BulletKit (EGM-2, Lonza). Cells used were between passages 3 to 12. Medium changes were performed every other day, and cells were split upon reaching 80% confluency.

Polyacrylamide (PAA) fabrication. PAA hydrogels were fabricated similarly to previously published protocols (56). Briefly, hydrogels with relative stiffnesses (Young's Modulus or elastic modulus, E) at 200 Pa, 480 Pa, 1 kPa, 2 kPa, 4.5 kPa, and 10 kPa were fabricated by mixing acrylamide from 40% stock solution (Sigma, A4058) with bis-acrylamide from 2% stock solution (Sigma, M1533) in phosphate buffer saline (PBS). Air bubbles introduced during mixing were removed by vacuum gas-purge desiccation for 30 min. The mixture was then mixed with 10% ammonium persulfate (Sigma, A3426) and tetramethylethylenediamine (Sigma, T7024) at a 1:100 and 1:1000 ratios, respectively, initiating PAA polymerization. The PAA mixture was then sandwiched between an 18-mm glass coverslip (Fisher) and a hydrophobically treated and dichlorodimethylsilane (Sigma, 440272)-coated glass slide. After 30 min of PAA polymerization, the 18-mm glass slide with the PAA hydrogel attached was carefully removed from the hydrophobic slide. Last, PAA hydrogels were functionalized with 0.2 mg/mL sulfosuccinimidyl-6-(4′-azido-2′-nitrophenylamino)-hexanoate (Pierce Biotechnology) followed by 10 mg/mL fibronectin.

Vascular patterning. GFP-HUVECs were seeded on fibronectin-coated PAA hydrogels at densities of 8×10^3 cells/cm^2, 1.4×10^4 cells/cm^2, and 2×10^4 cells/cm^2 and imaged on a Nikon Eclipse TE2000-U fluorescent microscope. The images were all processed using a custom-built image processing macro in FIJI2.

D. Image Analysis. The following processing is done in order to directly compare simulation predictions to experimental results (Figs. 4 and 5) and to obtain network metrics for simulations (Fig. 6 and *SI Appendix*, Figs. S9, S11, S12, and S17). All image analysis used in this work was carried out using the open-source software ImageJ (75). Raw grayscale experimental images are imported into ImageJ. "Enhance Contrast" command is run with "saturated pixels" widget set to 2. We then "Despeckle" the image and "Enhance Contrast" once more before running "Subtract Background" with a rolling ball radius of 50 pixels. We "Gaussian Blur" with a sigma of 10 pixels. We then threshold, keeping intensities 20 and above. This is then converted into a mask, skeletonized, and dilated four times so as to preserve the raw filling fraction (Fig. 4*B*).

For simulated networks like those shown in Fig. 2, we replace the isotropic disk markers with "pill-box" shaped markers (as seen in *SI Appendix*, Fig. S11) which are elongated along the dipole axis of each cell to guide the subsequent skeletonization. Using ImageJ, we first apply "Gaussian Blur" with a sigma of 2 pixels; then, we threshold keeping intensities 150 and above and then convert into a mask and skeletonize. Finally, we dilate the skeleton four times so that small-scale features of assembly like compact rings are preserved, while washing out the shape of the individual disks. At this point, both experimental and simulated images are dilated skeletons. The packing fraction of the dilated skeleton representations of simulations ($\tilde{\phi}$) are smaller than their respective nonoverlapping disk packing fraction (ϕ) by a factor, $\tilde{\phi} \approx 0.75\phi$. To compute fractal dimensions, we follow the aforementioned image processing with the additional step of dilating experimental skeletons so as to have roughly the same packing fraction as simulations We then use ImageJ's "Fractal box count" tool with the default pixel array.

To identify unique clusters in both experimental and simulation images, dilated skeleton images are imported into a custom python program. This program assigns a cluster label to the first nonzero pixel and then does recurrent loops assigning neighboring pixels to the same cluster label until a pixel is identified that does not neighbor any of the pixels with this cluster label. The cluster label is incremented and the process repeats until every nonzero pixel is assigned a cluster label.

Data, Materials, and Software Availability. All study data are included in the article and/or supporting information. The raw data has been deposited in the Dryad repository and can be found at https://doi.org/10.5061/dryad.kd51c5bcv (76).

ACKNOWLEDGMENTS. P.S.N. was supported by graduate fellowship funding from the NSF: NSF-CREST: Center for Cellular and Biomolecular Machines at the University of California (UC), Merced: NSF-HRD-1547848. P.S.N. and K.D. acknowledge support from the NSF (NSF-CMMI-2138672). A.G. acknowledges support from the NSF (NSF-DMS-1616926). We acknowledge support from the NSF-CREST: Center for Cellular and Biomolecular Machines at UC Merced (NSF-HRD-1547848, NSF-HRD-2112675) and the NSF Science and Technology Center for Engineering Mechanobiology award (NSF-CMMI-154857). We would like to thank Ulrich Schwarz and Samuel Safran for discussion in the early stages of the project, and the anonymous reviewers for important suggestions.

Author affiliations: [a]Department of Physics, University of California, Merced, CA 95343; and [b]Department of Materials and Biomaterials Science and Engineering, University of California, Merced, CA 95343

1. G. Forgacs, S. A. Newman, *Biological Physics of the Developing Embryo* (Cambridge University Press, 2005).
2. R. A. Foty, M. S. Steinberg, The differential adhesion hypothesis: A direct evaluation. *Dev. Biol.* **278**, 255–263 (2005).
3. D. Manoussaki, S. R. Lubkin, R. B. Vemon, J. D. Murray, A mechanical model for the formation of vascular networks in vitro. *Acta Biotheor.* **44**, 271–282 (1996). https://doi.org/10.1007/BF00046533.
4. A. Gamba *et al*., Percolation, morphogenesis, and burgers dynamics in blood vessels formation. *Phys. Rev. Lett.* **90**, 118101 (2003). https://link.aps.org/doi/10.1103/PhysRevLett.90.118101.
5. A. Szabo, E. D. Perryn, A. Czirok, Network formation of tissue cells via preferential attraction to elongated structures. *Phys. Rev. Lett.* **98**, 038102 (2007). https://link.aps.org/doi/10.1103/PhysRevLett.98.038102.
6. R. van Oers, E. Rens, D. LaValley, C. Reinhart-King, R. Merks, Mechanical cell-matrix feedback explains pairwise and collective endothelial cell behavior in vitro. *PLoS Comput. Biol.* **10**, e1003774 (2014).
7. N. Kleinstreuer *et al*., A computational model predicting disruption of blood vessel development. *PLoS Comput. Biol.* **9**, e1002996 (2013).
8. J. R. D. Ramos, R. Travasso, J. Carvalho, Capillary network formation from dispersed endothelial cells: Influence of cell traction, cell adhesion, and extracellular matrix rigidity. *Phys. Rev. E* **97**, 012408 (2018). https://link.aps.org/doi/10.1103/PhysRevE.97.012408.
9. D. Stepanova, H. M. Byrne, P. K. Maini, T. Alarcón, A multiscale model of complex endothelial cell dynamics in early angiogenesis. *PLoS Comput. Biol.* **17**, e1008055 (2021). https://pubmed.ncbi.nlm.nih.gov/33411727.33411727[pmid].
10. P. G. de Gennes, P. A. Pincus, Pair correlations in a ferromagnetic colloid. *Physik der Kondens. Materie* **11**, 189–198 (1970).
11. P. Ilg, E. Del Gado, Non-linear response of dipolar colloidal gels to external fields. *Soft Matter* **7**, 163–171 (2011). http://dx.doi.org/10.1039/C0SM00592D.
12. A. Kaiser, S. Babel, B. ten Hagen, C. von Ferber, H. Löwen, How does a flexible chain of active particles swell? *J. Chem. Phys.* **142**, 124905 (2015).
13. G. J. Liao, C. K. Hall, S. H. L. Klapp, Dynamical self-assembly of dipolar active brownian particles in two dimensions. *Soft Matter* **16**, 2208–2223 (2020). https://doi.org/10.1039/c9sm01539f.
14. N. Sakaï, C. P. Royall, Active dipolar colloids in three dimensions: Strings. Sheets, labyrinthine textures and crystals. arXiv [Preprint] (2020). http://arxiv.org/abs/2010.03925 (Accessed 1 December 2021).
15. F. Guzmán-Lastra, A. Kaiser, H. Löwen, Fission and fusion scenarios for magnetic microswimmer clusters. *Nat. Commun.* **7**, 13519 (2016), 10.1038/ncomms13519.
16. V. Telezki, S. Klumpp, Simulations of structure formation by confined dipolar active particles. *Soft Matter* **16**, 10537–10547 (2020). http://dx.doi.org/10.1039/D0SM00926A.
17. U. S. Schwarz, S. A. Safran, Physics of adherent cells. *Rev. Mod. Phys.* **85**, 1327–1381 (2013). https://link.aps.org/doi/10.1103/RevModPhys.85.1327.

18. I. B. Bischofs, U. S. Schwarz, Cell organization in soft media due to active mechanosensing. *Proc. Natl. Acad. Sci. U.S.A.* **100**, 9274–9279 (2003). https://www.pnas.org/content/100/16/9274.
19. R. J. Pelham, Y. l. Wang, Cell locomotion and focal adhesions are regulated by substrate flexibility. *Proc. Natl. Acad. Sci. U.S.A.* **94**, 13661–13665 (1997). https://www.pnas.org/content/94/25/13661.
20. M. Dembo, Y. L. Wang, Stresses at the cell-to-substrate interface during locomotion of fibroblasts. *Biophys. J.* **76**, 2307–2316 (1999). http://www.sciencedirect.com/science/article/pii/S0006349599773868.
21. N. Q. Balaban *et al*., Force and focal adhesion assembly: A close relationship studied using elastic micropatterned substrates. *Nat. Cell Biol.* **3**, 466 (2001). https://doi.org/10.1038/35074532.
22. M. Murrell, P. W. Oakes, M. Lenz, M. L. Gardel, Forcing cells into shape: The mechanics of actomyosin contractility. *Nat. Rev. Mol. Cell Biol.* **16**, 486 (2015). https://doi.org/10.1038/nrm4012.
23. C. A. Reinhart-King, M. Dembo, D. A. Hammer, Cell-cell mechanical communication through compliant substrates. *Biophys. J.* **95**, 6044–6051 (2008). http://www.sciencedirect.com/science/article/pii/S0006349508820188.
24. X. Tang, P. Bajaj, R. Bashir, T. A. Saif, How far cardiac cells can see each other mechanically. *Soft Matter* **7**, 6151–6158 (2011). http://dx.doi.org/10.1039/C0SM01453B.
25. I. Nitsan, S. Drori, Y. E. Lewis, S. Cohen, S. Tzlil, Mechanical communication in cardiac cell synchronized beating. *Nat. Phys.* **12**, 472–477 (2016).
26. J. Notbohm, A. Lesman, P. Rosakis, D. A. Tirrell, G. Ravichandran, Microbuckling of fibrin provides a mechanism for cell mechanosensing. *J. R. Soc. Interface* **12**, 20150320 (2015).
27. A. Abhilash, B. Baker, B. Trappmann, C. Chen, V. Shenoy, Remodeling of fibrous extracellular matrices by contractile cells: Predictions from discrete fiber network simulations. *Biophys. J.* **107**, 1829–1840 (2014). http://www.sciencedirect.com/science/article/pii/S000634951400931X.
28. D. E. Discher, P. Janmey, Y. l. Wang, Tissue cells feel and respond to the stiffness of their substrate. *Science* **310**, 1139–1143 (2005). http://science.sciencemag.org/content/310/5751/1139.
29. U. S. Schwarz *et al*., Calculation of forces at focal adhesions from elastic substrate data: The effect of localized force and the need for regularization. *Biophys. J.* **83**, 1380–1394 (2002). https://pubmed.ncbi.nlm.nih.gov/12202364.
30. J. D. Eshelby, The determination of the elastic field of an ellipsoidal inclusion, and related problems. *Proc. R. Soc. London. Ser. A Math. Phys. Sci.* **241**, 376–396 (1957). http://www.jstor.org/stable/100095.
31. I. B. Bischofs, U. S. Schwarz, Effect of Poisson ratio on cellular structure formation. *Phys. Rev. Lett.* **95**, 068102 (2005). https://link.aps.org/doi/10.1103/PhysRevLett.95068102.
32. A. Zemel, F. Rehfeldt, A. E. X. Brown, D. E. Discher, S. A. Safran, Optimal matrix rigidity for stress-fibre polarization in stem cells. *Nat. Phys.* **6**, 468 (2010). https://doi.org/10.1038/nphys1613.
33. A. J. Engler *et al*., Embryonic cardiomyocytes beat best on a matrix with heart-like elasticity: Scar-like rigidity inhibits beating. *J. Cell Sci.* **121**, 3794–3802 (2008). http://jcs.biologists.org/content/121/22/3794.
34. B. Friedrich, A. Buxboim, D. E. Discher, S. A. Safran, Striated acto-myosin fibers can reorganize and register in response to elastic interactions with the matrix. *Biophys. J.* **100**, 2706 (2011).
35. K. Dasbiswas, S. Majkut, D. E. Discher, S. A. Safran, Substrate stiffness-modulated registry phase correlations in cardiomyocytes map structural order to coherent beating. *Nat. Commun.* **6**, 6085 (2015).
36. K. Dasbiswas, H. Shiqiong, F. Schnorrer, S. A. Safran, A. D. Bershadsky, Ordering of myosin ii filaments driven by mechanical forces: Experiments and theory. *Philos. Trans. R. Soc. B: Biol. Sci.* **373**, 20170114 (2018). https://doi.org/10.1098/rstb.2017.0114.
37. I. B. Bischofs, S. A. Safran, U. S. Schwarz, Elastic interactions of active cells with soft materials. *Phys. Rev. E Stat Nonlin Soft Matter Phys.* **69**, 021911 (2004).
38. I. B. Bischofs, U. S. Schwarz, Collective effects in cellular structure formation mediated by compliant environments: A Monte Carlo study. *Acta Biomat.* **2**, 253–265 (2006). https://www.sciencedirect.com/science/article/pii/S1742706106000079.
39. D. E. Discher, P. Janmey, Y. l. Wang, Tissue cells feel and respond to the stiffness of their substrate. *Science* **310**, 1139–1143 (2005).
40. A. J. Engler, S. Sen, H. L. Sweeney, D. E. Discher, Matrix elasticity directs stem cell lineage specification. *Cell* **126**, 677–689 (2006).
41. O. Chaudhuri, J. Cooper-White, P. A. Janmey, D. J. Mooney, V. B. Shenoy, Effects of extracellular matrix viscoelasticity on cellular behaviour. *Nature* **584**, 535–546 (2020).
42. M. E. Asp *et al*., Spreading rates of bacterial colonies depend on substrate stiffness and permeability. *Proc. Natl. Acad. Sci. U.S.A. Nexus* **1**, pgac025 (2022).
43. D. Rüdiger *et al*., Cell-based strain remodeling of a nonfibrous matrix as an organizing principle for vasculogenesis. *Cell Rep.* **32**, 108015 (2020). https://www.sciencedirect.com/science/article/pii/S2211124720310007.
44. J. P. Califano, C. A. Reinhart-King, A balance of substrate mechanics and matrix chemistry regulates endothelial cell network assembly. *Cell. Mol. Bioeng.* **1**, 122 (2008).
45. K. Copenhagen *et al*., Frustration-induced phases in migrating cell clusters. *Sci. Adv.* **4**, eaar8483 (2018).
46. S. Bose, K. Dasbiswas, A. Gopinath, Matrix stiffness modulates mechanical interactions and promotes contact between motile cells. *Biomedicines* **9**, 428 (2021).
47. S. Bose, P. S. Noerr, A. Gopinathan, A. Gopinath, K. Dasbiswas, Collective states of active particles with elastic dipolar interactions. *Front. Phys.* **10**, 876126 (2022).
48. L. D. Landau, E. M. Lifshitz, *Theory of Elasticity, Course of Theoretical Physics* (Pergamon Press, London, 1959), vol. 7.
49. Y. Javanmardi, H. Colin-York, N. Szita, M. Fritzsche, E. Moeendarbary, Quantifying cell-generated forces: Poisson's ratio matters. *Commun. Phys.* **4**, 237 (2021).
50. D. Stauffer, Scaling theory of percolation clusters. *Phys. Rep.* **54**, 1–74 (1979).
51. F. Yonezawa, S. Sakamoto, M. Hori, Percolation in two-dimensional lattices. I. A technique for the estimation of thresholds. *Phys. Rev. B* **40**, 636–649 (1989). https://doi.org/10.1103/physrevb.40.636.
52. S. Kirkpatrick, Percolation and conduction. *Rev. Mod. Phys.* **45**, 574–588 (1973). https://doi.org/10.1103/revmodphys.45.574.
53. M. F. Sykes, J. W. Essam, Some exact critical percolation probabilities for bond and site problems in two dimensions. *Phys. Rev. Lett.* **10**, 3–4 (1963). https://doi.org/10.1103/physrevlett.10.3.
54. H. Schmidle, C. K. Hall, O. D. Velev, S. H. L. Klapp, Phase diagram of two-dimensional systems of dipole-like colloids. *Soft Matter* **8**, 1521–1531 (2011).
55. R. De, A. Zemel, S. A. Safran, Dynamics of cell orientation. *Nat. Phys.* **3**, 655 (2007). https://doi.org/10.1002/0471143030.cb1016s47.
56. J. R. Tse, A. J. Engler, Preparation of hydrogel substrates with tunable mechanical properties. *Curr. Protocols Cell Biol.* **47**, (2010). https://doi.org/10.1002/0471143030.cb1016s47.
57. R. Krishnan *et al*., Substrate stiffening promotes endothelial monolayer disruption through enhanced physical forces. *Am. J. Physiol.-Cell Physiol.* **300**, C146–C154 (2011).
58. E. M. Huisman, T. C. Lubensky, Internal stresses, normal modes, and nonaffinity in three-dimensional biopolymer networks. *Phys. Rev. Lett.* **106**, 088301 (2011). https://link.aps.org/doi/10.1103/PhysRevLett.106.088301.
59. A. Zaccone, Elastic deformations in covalent amorphous solids. *Mod. Phys. Lett. B* **27**, 1330002 (2013).
60. N. I. Petridou, B. Corominas-Murtra, C. P. Heisenberg, E. Hannezo, Rigidity percolation uncovers a structural basis for embryonic tissue phase transitions. *Cell* **184**, 1914–1928 (2021).
61. L. Papadopoulos *et al*., Comparing two classes of biological distribution systems using network analysis. *PLoS Comput. Biol.* **14**, e1006428 (2018).
62. H. Ronellenfitsch, E. Katifori, Global optimization, local adaptation, and the role of growth in distribution networks. *Phys. Rev. Lett.* **117**, 138301 (2016). https://link.aps.org/doi/10.1103/PhysRevLett.117.138301.
63. C. O. Crosby, J. Zoldan, Mimicking the physical cues of the ECM in angiogenic biomaterials. *Regener. Biomater.* **6**, 61–73 (2019). https://doi.org/10.1093/rb/rbz003.
64. B. N. Mason, A. Starchenko, R. M. Williams, L. J. Bonassar, C. A. Reinhart-King, Tuning three-dimensional collagen matrix stiffness independently of collagen concentration modulates endothelial cell behavior. *Acta Biomater.* **9**, 4635–4644 (2013). https://www.sciencedirect.com/science/article/pii/S1742706112003741.
65. A. J. Berger, K. M. Linsmeier, P. K. Kreeger, K. S. Masters, Decoupling the effects of stiffness and fiber density on cellular behaviors via an interpenetrating network of gelatin-methacrylate and collagen. *Biomaterials* **141**, 125–135 (2017). https://www.sciencedirect.com/science/article/pii/S0142961217304465.
66. D. B. Brückner *et al*., Learning the dynamics of cell–cell interactions in confined cell migration. *Proc. Natl. Acad. Sci. U.S.A.* **118**, e2016602118 (2021).
67. M. Scianna, C. Bell, L. Preziosi, A review of mathematical models for the formation of vascular networks. *J. Theor. Biol.* **333**, 174–209 (2013). http://www.sciencedirect.com/science/article/pii/S0022519313002117.
68. U. Doha *et al*., Disorder to order transition in cell-ECM systems mediated by cell-cell collective interactions. *Acta Biomater.* **154**, 290–301 (2022).
69. C. A. Reinhart-King, M. Dembo, D. A. Hammer, Endothelial cell traction forces on RGD-derivatized polyacrylamide substrata. *Langmuir* **19**, 1573–1579 (2003). https://doi.org/10.1021/la026142j.
70. D. A. Beysens, G. Forgacs, J. A. Glazier, Cell sorting is analogous to phase ordering in fluids. *Proc. Natl. Acad. Sci. U.S.A.* **97**, 9467–9471 (2000). https://www.pnas.org/content/97/17/9467.
71. M. Ghibaudo *et al*., Traction forces and rigidity sensing regulate cell functions. *Soft Matter* **4**, 1836–1843 (2008). http://dx.doi.org/10.1039/B804103B.
72. K. Mandal, I. Wang, E. Vitiello, L. A. C. Orellana, M. Balland, Cell dipole behaviour revealed by ECM sub-cellular geometry. *Nat. Commun.* **5**, 5749 (2014). https://doi.org/10.1038/ncomms6749.
73. D. Riveline *et al*., Focal contacts as mechanosensors: Externally Applied local mechanical force induces growth of focal contacts by an Mdia1-dependent and rock-independent mechanism. *J. Cell Biol.* **153**, 1175–1186 (2001). https://doi.org/10.1083/jcb.153.6.1175.
74. C. Stokes, D. Lauffenburger, S. Williams, Migration of individual microvessel endothelial cells: Stochastic model and parameter measurement. *J. Cell Sci.* **99**, 419–430 (1991). https://doi.org/10.1242/jcs.99.2.419.
75. C. A. Schneider, W. S. Rasband, K. W. Eliceiri, NIH image to ImageJ: 25 years of image analysis. *Nat. Methods* **9**, 671–675 (2012). https://doi.org/10.1038/nmeth.2089.
76. P. Noerr *et al*., Optimal mechanical interactions direct multicellular network formation on elastic substrates. Dryad. https://doi.org/10.5061/dryad.kd51c5bcv. Deposited 16 October 2023.